

Nanoscale

Accepted Manuscript



This is an *Accepted Manuscript*, which has been through the Royal Society of Chemistry peer review process and has been accepted for publication.

Accepted Manuscripts are published online shortly after acceptance, before technical editing, formatting and proof reading. Using this free service, authors can make their results available to the community, in citable form, before we publish the edited article. We will replace this *Accepted Manuscript* with the edited and formatted *Advance Article* as soon as it is available.

You can find more information about *Accepted Manuscripts* in the [Information for Authors](#).

Please note that technical editing may introduce minor changes to the text and/or graphics, which may alter content. The journal's standard [Terms & Conditions](#) and the [Ethical guidelines](#) still apply. In no event shall the Royal Society of Chemistry be held responsible for any errors or omissions in this *Accepted Manuscript* or any consequences arising from the use of any information it contains.



Journal Name

ARTICLE

Maximizing the photo catalytic and photo response properties of multimodal plasmonic Ag/WO_{3-x} heterostructure nanorods by variation of Ag size

Received 00th January 20xx,
Accepted 00th January 20xx

DOI: 10.1039/x0xx00000x

www.rsc.org/

Sirshendu Ghosh*, Manas Saha, Sumana Paul and S. K. De*

High quality nearly monodispersed colloidal WO_{3-x} nanorods of aspect ratio ~ 18 were synthesized using the thermal decomposition technique. Effects of capping agent and activating agent on nanorod aspect ratio have been studied. Excess carrier concentration due to large oxygen vacancy and smaller width of nanorods compared to Bohr exciton radius give rise to an increase of band gap. Shape anisotropy in nanorods results in two plasmonic absorbance bands at about 890 nm and 5900 nm corresponding to short axis and long axis plasmon mode. The short axis mode reveals excellent plasmonic sensitivity of ~ 345 nm per refractive index. A plasmonic photocatalysis process based on WO_{3-x} nanorods has been developed to synthesize Ag/WO_{3-x} heterostructure consisting of multiple Ag dots with ~2 nm size, randomly decorated on the surface of WO_{3-x} nanorods. Long time irradiation leads to an increase in size (5 nm) of Ag nanocrystal concomitant with decrease in number of Ag nanocrystals attached per WO_{3-x} nanorod. Plasmonic photocatalysis followed by thermal annealing produces only one Ag nanocrystal of size ~ 10 nm on each WO_{3-x} nanorod. Red shifting and broadening of plasmon bands of Ag nanocrystals and WO_{3-x} nanorods confirm the formation of heterostructure between metal and semiconductor. Detailed transmission electron micrographs analysis indicates the epitaxial growth of Ag nanocrystals onto WO_{3-x} nanorods. A high photocurrent gain of about 4000 is observed for Ag(10 nm)/WO_{3-x} heterostructures. The photodegradation rate for Rhodamine -B and Methylene blue is maximum for Ag(10 nm)/WO_{3-x} heterostructures due to efficient electron transfer from WO_{3-x} nanorods to Ag nanocrystals. Metal plasmon-semiconductor exciton coupling, prominent plasmon absorbance of metal nanoparticles, formation of epitaxial interface are found to be the important factors to achieve the maximum photocatalytic activity and fabrication of high speed photodetector device by employing the heterostructures.

Introduction:

In present scenario of nanoscience research, nanoscale metal/semiconductor hybrid heterostructures with various morphology and tunable sizes¹ are one of the most emerging candidates in multimodal biological detection², medical diagnostics³⁻⁵, light (solar) energy conversion⁶ especially in photocatalysis⁷ and optoelectronic devices⁸. In metal/semiconductor hybrid heterostructure, coupling between the quantum confined excitonic states of semiconductor and dielectrically confined electronic states in the metal part leads to a high electric polarizability at the plasmon frequency of the metal. This interaction enhances the physiochemical properties of wide band gap semiconductor or even generates new functionality. For example improved photocatalytic properties have been found for Au-ZnO¹, Au-CdSe⁹, Au-Bi₂S₃¹⁰, Au-SnS¹¹, Au-Cu₂ZnSnS₄¹² hybrid nanostructures. An important phenomenon of plasmonic-metallic

nanocrystals is their strong interaction with incident photon through excitation of localized surface plasmon resonance (LSPR). LSPR is collective oscillation of free electrons when the light frequency is resonant with the natural oscillation frequency of metal's free electrons in response to the restoring force of the positive nuclei. The optical absorption associated with LSPR varies significantly with the size of metal nanoparticles. So the presence of metal nanoparticle of different sizes in close vicinity of semiconductor nanocrystals can enhance the absorbance cross section of semiconductor induced by the increased electric field. For effective improvement of efficiency and speed in catalyst regain and optoelectronic devices based on metal-semiconductor heterostructure a strong exciton-plasmon coupling is essential to strengthen the interaction with light. A much easier and faster electron transfer occurs across the epitaxially grown interface between metal and semiconductor. Two types of electron transfer pathway are usually found for the fused metal-semiconductor structure: (i) electron can transfer from metal to semiconductor (ii) photogenerated electron of semiconductor can transfer to metal part shifting the plasmon frequency^{13,14} and promoting redox reactions^{15,16}. Of course the direction of electron transfer process depends upon the relative position of Fermi energy of the metal and semiconductor and their relative electron affinity.

Department of Materials Science, Indian Association for the Cultivation of Science, Kolkata-700032, India. Email: mssg2@iacs.res.in, msskd@iacs.res.in.

Electronic Supplementary Information (ESI) available: See

DOI: 10.1039/x0xx00000x

Literature study reveals that most of the metal-semiconductor heterostructures are ideal for harvesting the solar light in UV-VIS window. But in terms of available energy, visible (43%) and infrared (52%) light constitute most of the solar emission with very low amount of UV light. The greatest challenge for the maximum utilization of solar energy is to find a suitable non-toxic metal-semiconductor heterostructure which can absorb large amount of solar light in full solar spectrum. The combination of excitonic and plasmonic absorption of semiconductor and metal can be a probable way for enhancement of light energy conversion efficiency.

Tungsten oxide (WO_{3-x} , $0 < x < 1$), is an attractive semiconductor material with a wide band gap ranging from 2.6 to 3.0 eV depending on oxygen content. The value of band gap is ideal for light absorbance in both visible and infrared region. This oxide is of great interest because of its practical applications in smart windows¹⁷, photocatalysts^{18,19}, and gas/temperature sensors^{20,21}. Among the various phases in the WO_3 system, the nonstoichiometric phase (i.e. the WO_{3-x} form) has drawn much attention because of its unique structural property and the oxygen defects within its nanostructures. The intrinsic oxygen defects generate considerable amount of free electron in the material ($N \sim 10^{21} \text{ cm}^{-3}$) and a strong absorbance band was found in the Red to near infrared (NIR) region which was concluded as plasmonic absorbance band of WO_{3-x} by P. Alivisatos and his co-workers²².

It is well-known that one-dimensional structures can offer a direct path for the photogenerated charges, resulting in superior charge transport properties due to large surface area^{23,24}. So synthesis of semiconductor nanorod structures coupled with noble metal nanoparticles might be a promising candidate for photocatalysis and fabrication of photodetector. Herein we report the synthesis of new heterostructure materials composed of high quality bimodal plasmonic WO_{3-x} nanorods and variable size Ag nanoparticle. We use the plasmonic WO_{3-x} as the photocatalyst to generate Ag nanoparticles on the nanorod surface by in situ redox process in solution in presence of solar light irradiance. Ag particle size is varied with changing the light exposure time and little thermal annealing in solution. For the epitaxial Ag nanoparticle formation on the WO_{3-x} nanorods a moderate heat treatment is required. Moreover the size of noble metal Ag NC might play a vital role in metal/semiconductor heterostructure, as on decreasing the size of Ag NC a reduced absorption efficiencies and blue shift of LSPR peak energy was observed²⁵. Reduction of the size below 2-3 nm leads to the domination of size quantized electronic transition (semiconductor nature, quantum confinement effect) rather than the LSPR phenomenon²⁶. So it is important to study the influence of Ag NC size on metal/semiconductor heterostructure's performance to optimize the materials property for potential applications and also for basic understanding of electromagnetic interaction between metal and particular semiconductor nanocrystals.

Experimental section

Materials: All chemicals were used directly without further purification. Silver nitrate (ACS, 99.9%), Hexacarbonyltungsten [$\text{W}(\text{CO})_6$, 97%], 1-Octadecene (ODE, tech. 90%), Trimethylamine N-

oxide dihydrate (TMNO, 98%) were purchased from Alfa Aesar. Oleylamine (OLAM, tech., 70%), Oleic acid (OLAC, >99%), Hexadecylamine (HDA) were purchased from Sigma-Aldrich. Rhodamine -B (RhB), n-butylamine, Methylene blue (MB), ethanol, Tetrachloroethylene (TCE), hexane and other solvents were purchased from Merck India.

Synthesis of WO_{3-x} Nanorods (NR):

For the synthesis of WO_{3-x} nanorods (NR), 0.92 mmole of $\text{W}(\text{CO})_6$, 21 mmole of degassed OLAM and 6 mmole of TMNO were mixed together in a 25 ml round bottom flask equipped with a condenser. The mixture was stirred for 30 min to form slurry with dynamic evacuation. The flask was back-filled with dry N_2 and slowly heated to 100 °C with slow stirring. During the time of heating, a series of color change was observed from brown, pink, bluish green to white with frothing for the gradual change in oxidation state of W element. The white viscous gel was further heated to 140 °C, within 10 min the color changed to transparent blue. Finally the reaction mixture was gradually heated to 280 °C and reaction was carried out for 20 hrs at that temperature. The product was collected by centrifugation using 1:1 mixture of ethanol and acetone as non-solvent and hexane as solvent.

A size selective precipitation procedure has been followed to get better yield of nanorods. As we found nearly 80% of product is well defined high quality nanorods and rest of the product was nanowires and variable size nanorods. The products were dissolved in toluene and heated to 80 °C under constant stirring until the total product got dissolved. Acetone was added slowly to the solution till deep blue colored precipitate was appeared. The product was centrifuged and dried under vacuum for further characterization and applications.

Synthesis of Ag/ WO_{3-x} nanoheterostructure (NHS):

Ag/ WO_{3-x} nanoheterostructures (NHS) with variable size of Ag nanocrystals were synthesized by the photocatalytic reduction of Ag-amine complex by WO_{3-x} nanorods in toluene solvent. At first a stock silver solution was prepared by dissolving 1.2 mM AgNO_3 in 2 ml of OLAM in a vial with constant stirring at room temperature. Dissolution of AgNO_3 in OLAM is a slow process and the solution was occasionally sonicated. Once the mixture became transparent 5 ml toluene was added to Ag-OLAM solution with constant stirring. In another vial, 10 mg tungsten oxide nanorods were dissolved in 3 ml of toluene. Then 1.0 ml of Ag-OLAM solution in toluene was added and the system was degassed and backfilled with dry N_2 . The reaction vessel was exposed to the solar light irradiance of 0.65 Wcm^{-2} under constant stirring. Irradiation was performed for 1 hr. Aliquots were collected at different time interval and washed with an ethanol/toluene mixture by centrifugation process. The as-obtained grayish-blue product found to be highly soluble in organic solvents. For Ag(2nm)/ WO_{3-x} and Ag(5nm)/ WO_{3-x} NHSs synthesis, aliquots were taken at 30 min and 60 min respectively.

Ag(10nm)/ WO_{3-x} nanorods were synthesized via photocatalysis followed by thermal annealing process. In a typical synthesis,

photochemically synthesized 20 mg Ag(5 nm)/WO_{3-x} nanorods were dissolved in 4 ml of ODE and 0.2 ml of OLAM. The mixture was stirred for 30 min at room temperature under dynamic evacuation. Reaction vessel backfilled with dry N₂ and a continuous flow was maintained throughout the process. Reaction vessel was heated to 170 °C slowly and maintained for 30 min. The product was washed with ethanol/toluene mixture by centrifugation.

Characterization: The crystalline phases of the products were determined by X-ray powder diffraction (XRD) by using Bruker AXS D8SWAX diffractometer with Cu K_α radiation ($\lambda = 1.54 \text{ \AA}$), employing a scanning rate of 0.5° S⁻¹ in the 2 θ range from 20° to 80°. For XRD measurement the hexane solution of the NCs was drop cast over amorphous silicon sample holder till a naked eye visible thin layer was formed. Transmission electron microscopy (TEM) images, high angle annular dark field scanning TEM (HAADF STEM) images and energy dispersive spectrum (EDS) were taken using an Ultra-high resolution field emission gun transmission electron microscope (UHR-FEG TEM, JEM-2100F, Jeol, Japan) operating at 200 kV. For the TEM observations, the sample dissolved in hexane was drop cast on a carbon coated copper grid. The room temperature optical absorbance of the samples was recorded by a Varian Cary5000 UV-VIS-NIR spectrophotometer. Photoluminescence (PL) measurements were carried out at room temperature with a Fluorescence spectrometer (Hitachi, F-2500). Valence state analysis was carried out by using an X-ray photoelectron spectroscopic (XPS, Omicron, model: 1712-62-11) method. XPS measurement was done using an Al-K α radiation source under 15 kV voltage and 5 mA current. For XPS measurement the hexane solution of the NCs was drop cast over glass slide (2 mm \times 2 mm) till a naked eye visible thin layer was formed.

Photocatalytic Dye degradation study: The photocatalytic activities of the WO_{3-x} nanorods and Ag/WO_{3-x} heterostructures were studied by photodegradation of RhB and MB dyes in aqueous solution at room temperature. Prior to photocatalytic activity test, a ligand exchange reaction was performed to substitute long chain OLAM by n-butylamine. Ligand exchange procedure: hexane solution of nanorods or heterostructures were added to the n-butylamine solution in acetonitrile and jerked for few minutes. The butylamine capped samples were collected by centrifugation with excess acetonitrile. The butylamine capped NRs or NHSs were further annealed at 250 °C in Ar atmosphere.

For a typical dye degradation study of RhB, 20 mg of catalyst was added to the beaker containing 99 mL deionized water. After ultrasonication, Rh B dye (1 mL, 0.005 gm /L) was injected to above solution and the mixture was continuously stirred in dark for 1 hr to assure the establishment of an adsorption-desorption equilibrium. The mixture was exposed with light irradiance of 0.65 Wcm⁻² under constant stirring in ambient condition. The concentration of RhB during the degradation was monitored by absorbance study using a Varian Cary5000 UV-VIS-NIR spectrophotometer. For the study of MB degradation, same concentration as RhB (1 mL, 1 mmol/L) and similar experimental setup was followed.

Photoresponse study:

For the study of photoconductivity and photoresponse properties of the materials, a device was fabricated by spin casting the octane solution of nanorods and different heterostructures onto a patterned ITO coated glass substrate. At first 12 \times 12 mm² cleaned ITO coated glass substrate was etched at the middle using Zn dust/HCl to form a non-conducting area (approx. 6 \times 12 mm²) keeping the width of the ITO portion at two sides of nearly \sim 3 mm. These two ITO coated portions were adopted as two electrodes. Then the substrates were clean with water and alcohol respectively. Before use for coating, the substrate was flashed with high pressure dry N₂ gas. 0.5 ml octane solution of n-butylamine capped NRs/NHSs (concentration = 130 mg/ml) was spin casted over the etched area of substrate with a rotation speed of 3500 rpm. The ITO coated portion was cleaned with octane soaked cotton bud after each time of spin coating. Then the substrate was annealed at 250 °C for 2 hrs to remove the residual organic molecule from NRs/NHSs. The current-voltage (I-V) measurement between two electrodes was carried out by using Keithley Electrometer 6517A. The photocurrent was measured under illumination of light irradiance of 0.65 Wcm⁻² which was obtained by using Kratos universal Arc Lamp, Model 1152/1144 (150XE/200HG-XE). The time-resolved photocurrent measurement was carried out by illuminating the light for 15 s and then switching off the light for another 15 s periodically under an applied bias of 5 V. In all the experiments films were kept in a vacuum chamber with a transparent window.

Results and Discussion:

Fig.1(A) and (B) shows the large area TEM and high-angle annular dark field (HAADF) image of nearly monodispersed WO_{3-x} nanorods with 85 \pm 10 nm in length and 5.5 \pm 1.5 nm in width. The SAED pattern in Fig. 1(D) and XRD pattern in Fig. 2(A) confirms the crystal phase of WO_{3-x} as tetragonal with space group **p421m**. The diffraction peak positions at 23.05, 24.12, 47.34, 55.67 are assigned as the diffraction of (001), (020), (002), (240) planes (ICSD Code-86144). For the preferred growth of the nanorods along the c-axis the intensities coming from (001) and (002) planes are higher than that of others. Fig. 1(C) shows the HRTEM image of nanorods which confirm each nanorod as single-crystalline and grows along the [001] direction. The image shows the presence of mutual perpendicular (020) and (001) planes when viewed along $[\bar{2}00]$ zone axis. EDAX results indicate (ESI, Fig.S1) a large amount oxygen deficiency in the material.

The synthesis of WO_{3-x} NRs involved an oxidation process followed by nucleation and growth process. Here we used TMNO to oxidize W(0) to W(+5)/W(+6) states. The use of other oxidizing agent like N-methylmorpholine-N-oxide (NMO) is known as good oxidizing agent to synthesize semiconductor oxide nanocrystals²⁷ and is also effective to synthesize the sub-stoichiometric tungsten oxide nanorods. But the oxidation process occurred at much higher temperature (>180 °C) which was detected by change of the color of solution to blue and the resultant nanorods in the similar condition of reaction are thinner and poorly crystalline than TMNO based product (ESI, Fig. S2).

In presence of TMNO and OLAM, $W(CO)_6$ get dissolved by sequential color change to blue at 120 °C. The gradual color change is due to the gradual change of oxidation state of tungsten from 0 state to +6/+5 state. In presence of high amine concentration and water (coming from $TMNO \cdot 2H_2O$), W^{+6} might be present as ammonium salt of tungstic acid in blue color solution as we confirmed from FTIR analysis (ESI, Fig. S4). When we tried to isolate the compound by centrifugation with ethanol, we found a white color powdered compound. This was found to be an amorphous material when observed in TEM (ESI, Fig. S3). From previous study^{28,29}, it was well established that hydrated tungstic acid ($H_2WO_4 \cdot xH_2O$) has a lamellar structure and water molecule can be intercalated in between the two layers of tungstic acid. The water molecules are substitutable by alcohol or organic alkyl amine compound. So when the blue colored ammonium tungstate was washed with ethanol, ethanol is intercalated substituting the amine and water molecules. The white isolated intermediate product can be converted again to blue soluble one by treating it with any amine like butyl-amine.

In order to understand the growth process in depth, we studied the time dependent growth evolution by quenching the reaction at different stages and also studying the effect of nature of surfactant. It is well known that the precursor and nature of surfactant present have significant effects on both the size and morphology of nanocrystals. The blue colored transparent solution is stable up to 240 °C, and turbidity appeared above this temperature which indicates the start of formation of WO_{3-x} phase. Product collected at 260 °C shows [ESI, Fig. S5] the formation of nearly monodispersed nanorods with length 16.5 ± 1.5 nm and width 1.3 ± 0.3 nm. Fig. S5 shows the TEM images of product collected at different time interval (30 min, 2hr, 4hr and 6 hr) of reaction which reveals the gradual increase in rod length to 60 nm and width to 4.5 nm after 6 hrs of reaction. The growth rate along the longitude direction is much higher than along the width. According to the previous study^{30,31}, tungstic acid possesses a layered structure, which is made of distorted $WO_5(2H_2O)$ octahedron in a corner sharing mode. The $WO_5(H_2O)$ octahedra are connected with each other to form a $WO_3[H_2O]$ layer. The other half of water is located between such layers as interlayer water. The existence of interlamellar water can increase the spacing between the layer. The substitution of this water by amine or alcohol can control the spacing as well as decomposition of tungstic acid. The smaller sized amines like trimethyl amine or N-methyl morpholine can easily replace the H_2O molecules and weaken the chemical forces involved in the interlayer region. This lamellar hybrid intermediate decomposed at higher temperature into smaller layers to form the WO_{3-x} nuclei by combination of two octahedral W-O layers and removal of amines. The nuclei follow a growth along the c-axis resulting in nanorod structure, where the OLAM protects the edges. Scheme I shows a simplified model of intercalation of amine and different stage of nanorod growth. Use of different amine and acid as co-surfactant has a striking effect on nanorod width. When hexadecylamine (HDA) was used instead of OLAM, width of nanorods was found to be 16 ± 3 nm [ESI, Fig. S6] which is nearly 3 times of OLAM capped NRs with comparable length. The boiling point of HDA is lower than the reaction temperature, so the HDA are loosely bound to the surface of nanorods at reaction temperature and reversible adhesion-inadhesion equilibrium of HDA at the surface was there. So the inter-nanorod coupling process is operating to increase the width of nanorods³². In the present synthesis protocol, during the

decomposition of ammonium salt of tungstic acid oxygen containing ligand such as oleic acid has a strong influence on nanorods morphology. In presence of mixed surfactant (OLAM+OLAC) the width of nanorods increases at low concentration of OLAC [ESI, Fig. S7(A)] for inter nanorod coupling due to the poor surface protection by OLAC. At high concentration of OLAC, especially when the OLAC concentration is higher than OLAM nanobundles are found to be formed for higher degree of inter-rod coupling. In presence of only OLAC, no products are found to be formed, which proves the involvement of OLAM in reaction and product stabilization.

Fig. 1(E) shows the absorbance spectra of the nanorods in UV-VIS-NIR region in CS_2 solution. Spectra beyond 3300 nm were obtained from FTIR spectroscopy of nanorods due to the instrumental limitation of absorbance spectroscopy. The spectra composed of strong absorbance peaks at UV region, red-NIR region and IR region. The UV region absorbance is for inter-band absorbance. The band gap of the nanorods was obtained from Tauc plot in the energy range 3.25 eV to 4.25 eV as shown in the inset of Fig. 1(E). Two absorbance edges at 3.83 and 3.94 eV are found from the plot. These values are quite higher than the band gap of bulk non-stoichiometric tungsten oxide. The WO_{3-x} structure is a reduced form of cubic WO_3 that contains oxygen vacancies within crystal lattice. A huge amount of oxygen vacancy can generate free electrons which lift the Fermi level into conduction band region. The excess carrier concentration leads to an increase of band gap and the phenomenon is widely known as Burstein-Moss effect, frequently observed for aliovalent ion doped degenerate semiconductors^{33,34}. Again, if one or more than one of the dimensions of nanocrystals is smaller or comparable with its exciton Bohr radius, then the effective band gap energy might be higher than its bulk band gap for the quantum confinement effect^{35,27}. The width of the as-synthesized nanorods is smaller than the exciton Bohr radius of WO_3 ($R_{Bohr} = 13$ nm)³⁶. So one of the increased band gaps might be a result of strong quantum confinement effect.

To confirm whether the NIR absorbencies are for LSPR phenomenon of nanorods or for the charge transfer between defect states ($W^{+5} \rightarrow W^{+6}$, $O \rightarrow W^{+5}/W^{+6}$), we investigated absorbance spectra of nanorods in different solvents with varying refractive index. The LSPR maximum band position depends upon the dielectric medium in which it is dispersed. Normally the LSPR position shifts towards higher wavelength with increase of refractive index (RI) of solvent. Fig. 1(F) shows the change of absorbance peak maximum at red-NIR region with the variation of RI of the solvents and depicts a red shift with increase in solvent RI. This ensures that the absorbance band originates from the LSPR phenomenon. Semi-classical Drude model³⁷ predicts a similar dependence of peak position on RI as we observed from our experiment [ESI, Fig. S8(B)]. We were unable to study the same experiment with the highest intense absorbance band at 5690 nm (for CS_2 solvent) due to lack of instruments scope. Fitting of the experimental absorbance curve with the model results the charge carrier density of nanorods as $N = 6.1 \times 10^{21} \text{ cm}^{-3}$ and predicts a strong absorbance band at NIR region (5900 nm) [Details in ESI, Fig. S8(A)]. The experimentally observed higher wavelength peak is much broader than the calculated one compared to the case of shorter wavelength peak (red-NIR). The broadness of LSPR peak arises from several factors such as distribution of size and shape,

and damping of the plasmon arising from surface scattering of electrons³⁸. Larger size distribution for long axis (length 85 ± 10 nm) compare to the short axis (width 5.5 ± 1.5 nm) as obtained from TEM analysis also predicts the high broadness of the long axis absorbance peak. So the absorbance peaks at red-NIR (~ 900 nm) and NIR regions (~ 5690 nm) can be concluded as the short axis and long axis plasmon mode of nanorods respectively. The absorbance intensity for longitudinal mode of plasmon is found to be much higher than the transverse mode (short axis) from experimental data (Fig. 1E) but opposite phenomenon was observed from the calculated spectra based on semi-classical Drude model. This is quite expected for rod shaped plasmonic nanostructures^{39,40}, because the long axis mode couples strongly to the electromagnetic field. The nanorods demonstrate plasmonic sensitivity for the transverse mode (short axis mode) of roughly 345 nm per refractive index unit (nm/RIU) which is higher than the Ag nanoprisms⁴¹ (200 nm/RIU), Sn doped Zn-Cd-O nanocrystals (315 nm/RIU)³⁷ and comparable to those of Au nanoshells (130 to 360 nm/RIU)⁴² and spherical $\text{Cu}_2\text{-xS}$ (350 nm/RIU)⁴³. Semi-classical Drude model predicts much higher plasmonic sensitivity (~ 415 nm/RIU) than the experimental results. This difference can be attributed to the contribution of ligands attached to the surface of nanorods which makes the nanorods lesser expose to the solvent⁴⁴.

Fig. 2(A) shows the XRD pattern of pure and $\text{Ag}/\text{WO}_{3-x}$ NHSs with variable size of Ag NCs. The highest intense peak of (001) plane of tetragonal WO_{3-x} nanorods were present for all the heterostructures. Additionally two intense peaks at 38.05° and 44.1° for fcc-Ag (111) and Ag (200) are present in all the heterostructured NRs. These two peaks for $\text{Ag}(2\text{nm})/\text{WO}_{3-x}$ NHS are found to be very low intensity with respect to intensity of (001) plane of WO_{3-x} and quite broad. This is expected as the Ag NC's coherence length is in very small dimension (2 nm) and metal NC might be poorly crystalline as it is in cluster dimension. However these peaks for Ag NCs are more prominent for larger size (5 and 10 nm) Ag particles in $\text{Ag}/\text{WO}_{3-x}$ heterostructures.

The heterostructure formation was further characterized by optical absorbance spectroscopy and TEM analysis. Fig. 2(B) shows the absorbance spectra of WO_{3-x} NRs and different $\text{Ag}/\text{WO}_{3-x}$ heterostructures. The formation of the $\text{Ag}/\text{WO}_{3-x}$ heterostructures can be followed by observing the evolution of plasmonic band of the Ag NCs through a systematic reaction process. For the $\text{Ag}(2\text{nm})/\text{WO}_{3-x}$ NHSs, no such prominent peak for LSPR of Ag NCs was observed. However, the absorbance edge of WO_{3-x} was found to be red shifted and broadened up to 500 nm. Ag NCs which have dimension less than 2.5 nm does not show a prominent plasmon band as the permittivity of Ag is altered by quantum size effect²⁵ which normally results in a blue shift of plasmon band (compare to larger size NCs, ESI, Fig. S9) with reduced absorption efficiencies and broadening of line width. So the absorbance tail up to 510 nm for $\text{Ag}(2\text{nm})/\text{WO}_{3-x}$ NHS might be a result for the overlap of WO_{3-x} exciton band and broadened Ag plasmon band. A strong and prominent LSPR band for Ag NCs at 428 nm and 447 nm are found for $\text{Ag}(5\text{nm})/\text{WO}_{3-x}$ and $\text{Ag}(10\text{nm})/\text{WO}_{3-x}$ NHS respectively. Both the silver plasmon bands for the heterostructures are 30-50 nm red shifted compared to 8 nm OLAM capped Ag NCs in CS_2 [ESI, Fig. S9]. Alloying of Ag NCs with other metal can result in a red shift in LSPR band position due to lowering of electron concentration in the materials. Such possibility of alloy formation can be ignored in our

synthesized materials as no indication of alloy formation is observed in structural or TEM analysis. So the broadening and red shifting can be attributed to the semiconductor exciton-metal plasmon coupling phenomenon which is often found in metal-semiconductor heterostructures⁴⁵. Another important observation is that the strong plasmon band for short axis mode of WO_{3-x} NRs at 890 nm (in CS_2) is broadened and no sharp peak is observed in these two heterostructures. But from TEM observation (discussed in latter paragraph) the shape/size of the nanorods was found to be unchanged on heterostructure formation. This change of plasmon band structure of nanorods may be for change of dielectric constant of surroundings for Ag NC formation on surface or for plasmon-plasmon coupling between Ag NC and WO_{3-x} NRs. Such coupling often broadens or generates new plasmon bands at higher wavelength for charge-transfer or capacitive plasmon modes⁴⁶. Absorbances above 600 nm are for the plasmon absorbance of WO_{3-x} NRs for all the samples.

The as-synthesized heterostructures were further studied in details to understand growth process such as epitaxial growth. Fig. 3(A) and (B) shows the large area and closer view TEM image of $\text{Ag}(2\text{nm})/\text{WO}_{3-x}$ NHS, the product obtained after 30 min irradiance of $\text{Ag}(\text{OLAM})_2$ and WO_{3-x} solution. The NHSs were found to be well dispersed with minimum agglomeration. The formation of Ag clusters, size $\sim 2 \pm 0.5$ nm was found to be random onto surfaces of WO_{3-x} nanorods and no preferential growth on a particular surface or facet was observed. We could not establish an epitaxial formation of Ag from HRTEM analysis. Fig. 3 (C) and (D) show the TEM images of $\text{Ag}(5\text{nm})/\text{WO}_{3-x}$ NHSs. Fig 3(E) shows the HAADF image of heterostructures which clearly shows the formation of Ag NCs onto the surface of nanorods. The higher contrast part is for metal NCs. Fig. 3(F) shows the reconstructed HRTEM image of a part of the NHS where the heterostructure was found to be formed i.e. the sight of interest. Fig. 3(G) shows the FFT pattern obtained from Fig. 3(F). From the FFT pattern the calculated values of interplanar spacings (d) are found to be 0.236 nm and 0.37 nm which correspond to reflection of (111) plane of fcc Ag and (020) plane of tetragonal WO_{3-x} . The homogeneous growth of one facet of one material onto a particular facet of other or the formation of a plane of one material onto a particular plane of other material along the same direction with the minimal lattice mismatch leads to heterostructure formation between metal-semiconductor or semiconductor-semiconductor^{47,48}. The formation of Ag (111) plane along the same direction of (020) plane of WO_{3-x} proves the epitaxial growth of Ag onto WO_{3-x} . For better visualization the simulated HRTEM image considering only the epitaxial growth is shown in Fig. 3(H). Although the d-values of (111)Ag and (020) WO_{3-x} are not same or close but the $2 \times d_{(020)}$ of WO_{3-x} is nearly equal to $3 \times d_{(111)}$ of fcc Ag. Similar type observation was found by Pradhan and co-workers for Au-ZnSe and Au-Cu₂ZnSnS₄ heterostructures^{49,50}.

Fig. 4 (A) shows the large area TEM image of $\text{Ag}(10\text{nm})/\text{WO}_{3-x}$ heterostructures which indicates the higher contrast Ag NCs attached with almost all of the NRs. Fig. 4(B) displays the HRTEM image of a single $\text{Ag}/\text{WO}_{3-x}$ heterostructure at the site of interest where the epitaxy is expected to be observed. Fig. 4(C) shows the FFT pattern obtained from the green square area of Fig. 4(B), i.e. the pure WO_{3-x} region. The indexed planes from the FFT-spot are (021), (020) and (001) when viewed from $[\bar{2}00]$ direction of the tetragonal WO_{3-x} NRs, which confirm no change of phase of WO_{3-x}

upon photocatalysis followed by heat treatment. Fig. 4(D) shows the atomic model of tetragonal WO_{3-x} along $[\bar{2}00]$ direction. Fig. 4(E) shows the FFT pattern obtained from the blue color square area of Fig. 4(B). The spots appeared in FFT are originated from planes of both Ag and WO_{3-x} phases. The d-value obtained from the orange circled spot which is also along the direction of (020) plane of WO_{3-x} (highlighted in yellow circles) is found to be 0.236 nm, which is the reflection of the fcc Ag (111) plane. The growth of the (111) Ag plane along the same direction of (020) plane of WO_{3-x} proves the formation of epitaxy between these two planes. Fig. 4(F) shows the simulated HRTEM image by masking the highlighted two spots in Fig. 4(E) which also clearly shows the epitaxy along the [001] direction of WO_{3-x} NRs. The yellow and orange colored lines are indicated for WO_{3-x} and Ag part respectively for better visibility of coincidence of planes. The epitaxy formation can be concluded by matching $3 \times d(111)$ Ag (= 0.708 nm) with the $2 \times d(020)$ WO_{3-x} (= 0.72 nm) as we also observed for Ag(5nm)/ WO_{3-x} NHSs. Fig. 4 (G) and (H) show atomic arrangement of (020) planes of WO_{3-x} and (111) planes of Ag and matching between $2d(020)$ and $3d(111)$ planes.

The detailed growth mechanism study for the formation of metal-semiconductor oxide heterostructure is very rare in literature. So it is important to study the growth mechanism of WO_{3-x} based heterostructures. Ag/ WO_{3-x} heterostructured NRs were synthesized by using the plasmonic photocatalysis process. Here WO_{3-x} NRs acts as the plasmonic photocatalyst. Due to the presence of high electron concentration ($N = 6.1 \times 10^{21} \text{ cm}^{-3}$) due to large oxygen vacancy, the NRs shows a strong bimodal plasmonic absorbance in Vis-NIR region. In recent years, many experimental researches proved that the plasmonic NCs may act as reducing agent in chemical reactions^{44,45}. For the selective formation of Ag NCs onto WO_{3-x} NRs we took advantage of light excited energetic electron transfer from plasmonic oxide nanorods in presence of light to reduce Ag(I)-OLAM complex directly on the nanorod surface. Under light illumination, the electric field near the tip and edges of WO_{3-x} NRs enhances due to strong plasmon band in red and NIR region. The energetic electrons (or carriers) in the presence of intense electric field can decay and produce energetic charge carriers in the NRs^{51,52}. Also the enhanced electric field might accelerate the transfer of excited charge carriers to the close surroundings or absorbent for NRs. When Ag(I)(OLAM)₂ complex was mixed with WO_{3-x} NRs in toluene under irradiance of light Ag(I) ions closer to the surface of NRs get reduced to Ag(0) nuclei.

The reaction rate or conversion efficiency depends upon the intensity of light irradiance for plasmonic catalysis induced reduction process, the phenomenon mainly established by S. Linc and his co-workers^{53,54}. To confirm whether the catalytic reduction of Ag(I) by WO_{3-x} is influenced by plasmonic property of latter, we carried out the same reaction for a particular time duration at different light irradiance intensities (standardized with a photometer). Fig. 5 shows plot of Ag LSPR absorbance peak intensity with different light irradiance intensity. The inset shows the gradual increase of LSPR peak intensity with increase in light irradiance intensity. The almost linear dependence of Ag LSPR intensity (which is also the rate of formation of Ag NCs) with the light power density clearly indicates that the LSPR property of WO_{3-x} NRs plays a vital role in light driven catalytic process.

At the early stage of light irradiance, the 30 min reaction products show the presence of large amount of Ag NCs with small dimension around the surface of each nanorods. But the prolonged time irradiance (60 min) results the heterostructures where the number of Ag NCs situated with each rod are lower but the size become nearly double. Long time irradiance leads to the more reduction reaction of Ag^+ which results the gradual growth of some of the existing Ag NCs on WO_{3-x} NRs. Some of the existing Ag NCs (which are smaller in size) might undergo oxidation to Ag(I) which can be released to solution or reside onto the surface of WO_{3-x} NRs, which leads to the decrease in number of Ag NCs embedded per WO_{3-x} NRs compare to 30 min reaction product. The oxidation of small sized Ag NCs is feasible as they are more energetically unstable and also the oxidation can be done by W^{+6} ions in WO_{3-x} as both W^{+5} and W^{+6} are stable valence state in WO_{3-x} structure [see ESI, Fig. S10, XPS analysis] and interchangeable by polaron hopping⁵⁵. The released electrons can go to either the W site or transfer to the growing site of Ag NCs (as metal can act as electron sink) through the WO_{3-x} NRs (along the c-axis) by the hopping process. Large amount of surface vacancy states are present in the as-synthesized WO_{3-x} NRs (as evidenced from the generation of LSPR), which can participate in electron transfer to larger size Ag NCs.

More interesting observation was found for the plasmonic photocatalysed followed by thermally treated product. For Ag(10 nm)/ WO_{3-x} NRs, each of the NRs are epitaxially connected with only one Ag NC with size ~ 10 nm. This indicates that the annealing at 170 °C leads to an increase in Ag NC volume with decrease in number of Ag NC situated at each NR. During the thermal treatment no extra Ag(I) source or ex-situ synthesized Ag NCs was added. So the increase of Ag NC volume might be accompanied with decrease in volume of other Ag NCs. A similar type observation was previously reported by L. Manna and his co-authors for Au-CdSe heterostructure formation⁴⁸. For that case, small Au dots close to the tip region of nanorod migrate along the rod surface and they finally merged with the larger Au NC at the tip. They explained the phenomenon by combination of atomic and cluster diffusion mechanism. They carried out the synthesis in inert atmosphere and in solid state unlike us where we used OLAM and ODE for making Ag(5nm)/ WO_{3-x} NHS soluble before annealing. We can speculate an ionic diffusion process in the present case. Fig. S11 in ESI shows the TEM images of product collected after 10 min of reaction at 170 °C. After few seconds of exposure to the electron beam during TEM imaging, surface/edge structure of NRs were found to be changed. Reconstructed HRTEM image from the surface of the NRs shows the formation of Ag(111) planes. WO_3 can be described as a modification of perovskite-type ABO_3 lattice^{56,57} in which the A site is unoccupied and B-site is occupied by W atoms, as shown in the Fig. 6. This crystal structure is generally composed of WO_6 octahedra as the basic structural unit, forming one dimensional tunnel of variable sizes and shapes⁵⁸. Cations can be intercalated to the pseudo-A site if the sizes match well with the hole. Ag(I) having ionic radius of $r_{\text{ionic}}^{\text{Ag}^+} = 115$ pm can fit into the size of one-dimensional tunnel of tetragonal WO_{3-x} ^{58,59}. So upon oxidation of Ag(0) to Ag(I) in small size Ag NCs, the Ag^+ ions can be trapped into the crystal structure (A-site) instead of going to the solution. When the product was collected at intermediate time and exposed with electron beam in TEM, formation of small Ag cluster was found onto the surface. Complete reaction product at 30 min does not show any Ag cluster formation upon exposure with electron beam. So at the beginning of thermal treatment Ag(0) is oxidized to Ag(I)

which is intercalated at the A-site. On progress of reaction Ag(I) moves to the larger Ag NC attached to rod and is deposited there. To validate this conjecture we performed two more experiments. First: we used thin nanrods (width < 3 nm, byproduct of the reaction) composed of some nanowire for the plasmonic catalysis followed by thermal treatment, the major product was found to be Ag/Ag₂WO₄ nanoheterodimer. Details explanation of TEM images is given in supporting information Fig.S12. This phase transition from WO_{3-x} to Ag₂WO₄ is only possible if Ag(I) ions got intercalated in A-site during the annealing process. Second: we tried to synthesize Au/WO_{3-x} heterostructure by similar process (only the photocatalysis step) we observed that Au cluster was formed at the near surface area of rods with fewer number of Au(0) on the rods [ESI, Fig.S13]. This proves that the plasmonic photocatalysis process is also operative to reduce Au³⁺ to Au(0). On annealing the sample in similar way as described for Ag(10nm)/WO_{3-x} NRS we found larger gold NCs which were detached from the NRs[ESI, Fig.S13]. Au³⁺ which has higher ionic radii ($r_{\text{ionic}}^{\text{Au}^{3+}} = 137 \text{ pm}$) than Ag(I) does not fit into the A-site, i.e. Au³⁺ is not intercalated during plasmonic photocatalysis and annealing. Larger size Au NCs on annealing is formed due to the ostwald ripening of small Au NCs. So intercalation of Ag(I) ions through the one-dimensional tunnel in tetragonal WO_{3-x} crystal structure is found to be the key factor for Ag/WO_{3-x} heterostructure formation.

Formation of metal-semiconductor heterostructures often generates new physical property or modifies the materials properties. Depending upon the energy band structure of metal and semiconductor the Fermi energy level (E_F) of semiconductor can bend upwards or downwards to equilibrate the Fermi level. Here we studied the photo response property and photocatalytic efficiencies of dye-degradation of the materials to understand the effect of formation of heterostructure and Ag NCs size on materials photophysical properties.

The photodetector devices were first fabricated by spin casting the NRs and metal NR heterostructures onto a patterned ITO substrate and their photoresponse properties were investigated by using a light source with an irradiance of 0.65 W/cm². Fig. 7 shows the I-V plot (left panel) both in presence (LIGHT) and absence (DARK) of light in the voltage range -5 V to +5 V and time dependent photoresponse curve (right panel) at bias voltage 5V (time lapse = 15 s, ON = irradiation on; OFF = irradiation off) for the photodetectors made from pure WO_{3-x} NRs and all the Ag decorated WO_{3-x} heterostructures. The non-linear I-V curves prove non-ohmic type contact. The photocurrent (I_{photon}) values for all the devices are higher than the dark current (I_{dark}) values at all bias voltages. The photocurrent gain which is the ratio of I_{photon} and I_{dark} is found to be maximum for Ag(10nm)/WO_{3-x} heterostructures (~4000) and have much higher value than Ag (5nm)/WO_{3-x} (~110), Ag (2nm)/WO_{3-x} (~9.5) and WO_{3-x} (~5) NRS. The photocurrent gain value for WO_{3-x} NRs and Ag(2nm)/WO_{3-x} heterostructure does not differ significantly. But a strong effect of Ag (2nm) NC decoration is found on the structure of response curve depicted in right panel of Fig.7. Both the photocurrent and dark current for all the Ag decorated WO_{3-x} NRs are quite stable and response curves are repeatable for more than 30 cycles. The pure WO_{3-x} device shows a different response curve structures. The photo and dark current values increase with the number of cycle repetition and produce an stair like shape. As-synthesized WO_{3-x} NRs containing large amount of

oxygen vacancies can trap electrons which cannot participate in electrical conduction. The presence of trapped states can reduce electron-hole pair recombination rate and may improve the performance of device. When the sample is irradiated with light in the next cycle the trapped electrons in oxygen vacancy sites can jump to conduction band (CB) and consequently increases photocurrent value. Such increase of photocurrent continues until all trap sites are occupied by photoexcited electrons.⁶⁰ As a result photocurrent value increases with time. But with Ag decoration on NRs, the improved photo stability of devices was observed. This observation can be explained by studying the relative band alignment of WO₃ and Ag. The position of Fermi level of Ag ($E_F = -4.7 \text{ eV}$) is below the conduction band edge of WO_{3-x} (shown in Fig.8)⁶¹. So effective electron transfer can occur from the CB of WO_{3-x} to the E_F of Ag. As a result, Ag NCs can act as an electron sink to capture electron which is produced during photoexcitation and decreases of recombination of electron and holes (increase in exciton lifetime) and can effectively transfer electrons to the electrode. Also the presence of Ag NCs onto the surface of WO_{3-x} NRs decreases the number of accumulated electrons in oxygen vacancy sites on repeated light exposure cycles, as the E_F of Ag is closely situated with the CB and defects states are normally resides in deep in the band gap. This explanation is also supported by the observation that defect PL of pure WO_{3-x} got quenched with Ag NC attachment [ESI, Fig.S14].

For a fast and stable photodetector, two major criteria are (i) increase of lifetime of exciton pair, i.e. complete separation of e^- and h^+ , and (ii) fast recombination of e^- and h^+ pair in absence of light. First factor increases the photocurrent gain value and the second one decreases the response time which makes the device fast. Pure WO_{3-x} shows a slow decay of photocurrent in absence of light. But other Ag/WO_{3-x} heterostructures specially Ag(5nm) and Ag(10nm)/WO_{3-x} samples shows a fast gain and fast decay of current in presence and absence of light. The response time (time require to gain 90% of maximum photocurrent) for both this sample was found to be just 1 sec. Another interesting observation is that the photocurrent gain value increases with increase in Ag NCs size. The 5 nm and 10 nm Ag/WO_{3-x} NRs shows photocurrent gain value 110 and 4000 respectively. In both these heterostructures we found prominent plasmon band for Ag NC and Ag-WO_{3-x} epitaxial connection. The prominent LSPR band for Ag NC results in increase of absorbance efficiency of visible light of the heterostructure NRs and an epitaxial interface between metal and semiconductor leads to effective charge transfer from semiconductor to metal. Also the plasmon (metal)-plasmon (semiconductor) coupling might increase the absorbance efficiency at NIR region. But for the Ag(2nm)/WO_{3-x} sample, Ag NCs does not show a prominent LSPR band and unable to absorb the visible light efficiently. But it can stabilize the photocurrent value by charge transfer phenomenon.

As the WO_{3-x} has a rod-like shape, having a large surface area, capable of transferring charge along the c-axis with high concentration of oxygen vacancy, we expect the materials are promising for photocatalytic application. We choose RhB and MB as the model dyes under light illumination (0.65 W/cm²). The changes of RhB and MB concentration were monitored by measuring the optical absorbance at 553 nm and 662 nm respectively of the suspension at 5 min time interval [ESI, Fig. S15]. The absorbance spectrum of both RhB and MB does not show any apparent change

in absorbance in absence of any catalyst even with long time exposure to light. The photodegradation of RhB and MB in presence of WO_{3-x} nanorods is found to be relatively slow with just ~20% of RhB and ~35% of MB degraded after 30 min of illumination (Fig.9). Significantly higher percentages of RhB and MB are degraded in presence of Ag/ WO_{3-x} heterostructures. Nearly 80%, 91% and 98% of RhB are found to be degraded in presence of Ag(2nm)/ WO_{3-x} , Ag(5nm)/ WO_{3-x} and Ag(10nm)/ WO_{3-x} heterostructure respectively in 30 min of irradiance. In case of MB, the degradations are 67%, 89% and 95% in the presence of above mentioned catalyst in light illumination. So both the RhB and MB are found to be more than 95% degraded in presence of Ag(10nm)/ WO_{3-x} nanoheterostructures in a short period of time. We also estimated the reaction rate for each individual process. The photoreduction kinetics of both RhB and MB follows a pseudo first order kinetics, expressed by, $\ln(C_0/C) = Kt$, where C_0 is the concentration of dye at equilibrium established at dark condition and C is the concentration of nondegraded dye after different time intervals of irradiance and K is the apparent rate constant⁶². Figs. 9 (C) and (D) show the plots of $\ln(C_0/C)$ vs t for RhB and MB dyes. Ag(10nm)/ WO_{3-x} heterostructures reveal the highest rate constant $K_4 = 0.133 \text{ min}^{-1}$ about 15 times and 2 times higher than that of pure WO_{3-x} ($K_1 = 0.0085 \text{ min}^{-1}$) and Ag(2nm)/ WO_{3-x} ($K_3 = 0.057 \text{ min}^{-1}$) respectively. Whereas for MB dye degradation rate constant for Ag(10nm)/ WO_{3-x} catalyst is 0.094 min^{-1} nearly 6 times than WO_{3-x} catalyst and 2.5 times than Ag(2nm)/ WO_{3-x} heterostructure. So, an increase in rate constant value of RhB dye degradation in presence of heterostructure is relatively higher than that for MB dye degradation. This discrimination might be for the difference in adsorption of dyes in heterostructure surface and also depends upon the relative energy states of dyes with respect to the WO_{3-x} and Ag¹¹. All the heterostructures are efficient light absorber in UV, VIS and NIR region due to excitonic band and plasmon absorption and plasmon-plasmon coupling. Also the complete separation of opposite charge pair (electron and hole) at the nanostructure surface is another reason for a good photocatalytic activity. Moreover for better understanding the photocatalysis mechanism, we have estimated the Ag weight percentage in different Ag/ WO_{3-x} heterostructures by atomic absorption spectroscopy (AAS). Ag weight percentage was found to be ~ 5 %, 14.2 % and 14.9 % in 2 nm, 5 nm and 10 nm Ag decorated heterostructures. The weight % increment from 5 nm to 10 nm Ag/ WO_{3-x} was not so remarkable (as no ex-situ synthesized Ag NC/ Ag precursor was added during the annealing of Ag(5nm)/ WO_{3-x} sample) but the rate constant of RhB dye degradation was found to be ~1.52 time higher for 10 nm Ag system than 5 nm Ag decorated heterostructure. So epitaxy formation between Ag and WO_{3-x} NR, strong LSPR absorbance efficiency of 10 nm Ag nanocrystals have played the most critical role in this Ag decorated heterostructure system.

Non-stoichiometry in WO_{3-x} nanorods, high surface area⁶³, and unsaturated oxygen co-ordination are favorable for adsorption of oxygen and H_2O molecules⁶⁴. When the heterostructure are illuminated with light, incident photons are absorbed by Ag NCs embedded on the surface of nanorods. Simultaneously, band gap excitation of WO_{3-x} by photon absorption leads to the formation of photoelectrons in conduction band (CB) with concurrent generation of same amount of holes in valence band (VB). The photoexcited electrons would transfer from WO_{3-x} to Ag NCs for the lower Fermi energy level of Ag (Fig.8) and higher electron affinity of metal. Hence the proper band alignment across metal-semiconductor

junction favors the separation of electron and hole. The rate of photoelectron transfer from CB of WO_{3-x} to metal depends upon the nature of contact between WO_{3-x} and Ag. An epitaxial interface between metal and semiconductor always accelerates the photoelectron transfer process. The Ag/ WO_{3-x} heterostructures can absorb light in a wider wavelength region (as we found in absorbance spectra) from UV to NIR which gives rise to a larger number of photoexcited electrons and holes compare to the pure WO_{3-x} NRs. The photoelectrons present on the surface can react with O_2 to form superoxide radical anion (O_2^-) and separated holes can react with H_2O to form highly reactive hydroxyl radical (OH^\cdot). Thus superoxide and hydroxyl radicals can directly degrade the organic dyes. The highest catalytic activity of Ag(10nm)/ WO_{3-x} heterostructures compare to the other should be for the high light absorbance efficiency in VIS region for predominant LSPR band of Ag NCs and complete charge separation.

Conclusions

In summary, we successfully synthesized nearly monodispersed plasmonic WO_{3-x} nanorods by successive intercalation of amine and thermal decomposition of in-situ formed tungstic acid. Large amount of oxygen vacancy and high aspect ratio of nanorods give rise to strong NIR (~900) nm and mid-IR (~6000 nm) plasmonic absorbances. Moreover we successfully fabricated Ag/ WO_{3-x} heterostructures by implementing the plasmonic photocatalysis process of WO_{3-x} nanorods under illumination. Intercalation and diffusion of Ag(I) ions through open channels of WO_{3-x} assist the formation of Ag nanocrystal. Minimum lattice mismatch between periodic arrangement of 3 (111) plane of Ag with 2 (020) planes of WO_{3-x} leads to an epitaxial growth of Ag/ WO_{3-x} heterostructure. Open structure of WO_{3-x} , oxygen vacancy, epitaxial junction, accurate band alignment between metal and semiconductor and light absorption over a wide spectral range significantly improve the photocurrent gain (1000 times) and photocatalytic activity (25 times). The size of Ag nanocrystals plays an important role to enhance the performance of photodetector and photocatalyst. Our synthesis technique demonstrates a promising wet chemical route to design good quality interface between metal and semiconductor nanostructures for exotic applications in photochemical and optoelectronic devices. Again, these as-synthesized Ag/ WO_{3-x} heterostructures seems to be applicable in other photon induced material properties like surface enhanced Raman spectroscopy, gas sensing, catalytic combustion, plasmon induced chemical transformation in organic synthesis etc. Additionally our demonstrated synthesis technique also opened up a new synthesis process of colloidal Ag/ $\alpha\text{-Ag}_2\text{WO}_4$ heterostructure (according to our knowledge it is not ever reported). Further extensive studies regarding the photophysical properties of this heterostructure are currently underway in our laboratory.

Acknowledgements

The authors S. G and S. P acknowledge CSIR, India and DST INSPIRE fellowship respectively for providing the fellowships during the tenure of the work.

Notes and references

- M. N. Tahir, F. Natalio, M. A. Cambaz, M. Panthöfer, R. Branscheid, U. Kolb and W. Tremel, *Nanoscale*, 2013, **5**, 9944.
- X. Huang, I. H. El-Sayed, W. Qian and M. A. El-Sayed, *J. Am. Chem. Soc.*, 2006, **128**, 2115.
- A. K. Salem, P. C. Searson and K. W. Leong, *Nat. Mater.*, 2003, **2**, 668.
- M. I. Shukoor, F. Natalio, M. N. Tahir, M. Wiens, M. Tarantola, H. A. Therese, M. Barz, S. Weber, M. Terekhov, H. C. Schröder, W. E. G. Müller, A. Janshoff, P. Theato, R. Zentel, L. M. Schreiber and W. Tremel, *Adv. Funct. Mater.*, 2009, **19**, 3717.
- S. Wang, A. Riedinger, H. Li, C. Fu, H. Liu, L. Li, T. Liu, L. Tan, M. J. Barthel, G. Pugliese, F. D. Donato, M. S. D'Abbusco, X. Meng, L. Manna, H. Meng and T. Pellegrino, *ACS Nano*, 2015, **9**, 1788.
- P. V. Kamat, *J. Phys. Chem. C*, 2008, **112**, 18737.
- V. Subramanian, E. E. Wolf and P. V. Kamat, *J. Am. Chem. Soc.*, 2004, **126**, 4943.
- Y. Shemesh, J. E. Macdonald, G. Menagen and U. Banin, *Ang. Chem. Int. Ed.*, 2011, **50**, 1185.
- K. K. Haldar, G. Sinha, J. Lahtinen and A. Patra, *ACS Appl. Mater. Interfaces*, 2012, **4**, 6266.
- G. Manna, R. Bose and N. Pradhan, *Ang. Chem. Int. Ed.*, 2014, **53**, 6743.
- B. K. Patra, A. K. Guria, A. Dutta, A. Shit and N. Pradhan, *Chem. Mater.*, 2014, **26**, 7194.
- X. Yu, A. Shavel, X. An, Z. Luo, M. Ibáñez and A. Cabot, *J. Am. Chem. Soc.*, 2014, **136**, 9236.
- T. Hirakawa and P. V. Kamat, *Langmuir*, 2004, **20**, 5645.
- L. Carbone, A. Jakob, Y. Khalavka and C. Sönnichsen, *Nano Lett.*, 2009, **9**, 3710.
- R. Costi, A. E. Saunders, E. Elmalem, A. Salant and Uri Banin, *Nano Lett.*, 2008, **8**, 637.
- E. Elmalem, A. E. Saunders, R. Costi, A. Salant and U. Banin, *Adv. Mater.*, 2008, **20**, 4312.
- C. Yang, J-F. Chen, X. Zeng, D. Cheng and D. Cao, *Ind. Eng. Chem. Res.*, 2014, **53**, 17981.
- K. Sayama, K. Mukasa, R. Abe, Y. Abeb and H. Arakawa, *Chem. Commun.*, 2001, 2416.
- J. Liu, O. Margeat, W. Dachraoui, X. Liu, M. Fahlman and J. Ackermann, *Adv. Funct. Mater.*, 2014, **24**, 6029.
- L. Xu, M-L. Yin and S. Liu, *Sci. Rep.*, 2014, **4**, 6745.
- L.F. Reyes, A. Hoel, S. Saukko, P. Heszler, V. Lantto, C.G. Granqvist, *Sens. Actuators, B* **2006**, **117**, 128.
- K. Manthiram and A. P. Alivisatos, *J. Am. Chem. Soc.*, 2012, **134**, 3995.
- Wu, Y.; Xi, Z.; Zhang, G.; Yu, J.; Guo, D. *J. Cryst. Growth*, 2006, **292**, 143.
- S. J. Yoo, Y. J. Lim, Y. E. Sung, Y. H. Jung, H. G. Choi, D. K. Kim, *Appl. Phys. Lett.*, 2007, **90**, 173126.
- J. A. Scholl, A. L. Kohand J. A. Dionne, *Nature*, 2012, **483**, 421.
- H. Xu and K. S. Suslick, *Adv. Mater.*, 2010, **22**, 1078.
- S. Ghosh, K. Das, K. Chakrabarti and S. K. De, *Dalton Trans.*, 2013, **42**, 3434.
- L. Liang, J. Zhang, Y. Zhou, J. Xie, X. Zhang, M. Guan, B. Pan and Y. Xie, *Sci. Rep.*, 2013, **3**, 1936.
- M. Imperor-Clerc, D. Bazin, M-D. Appay, P. Beaunier and A. Davidson, *Chem. Mater.*, 2004, **16**, 1813.
- H. Zheng, J. Z. Ou, M. S. Strano, R. B. Kaner, A. Mitchell and K. Kalantar-zadeh, *Adv. Funct. Mater.*, 2011, **21**, 2175.
- Y.M. Li, M. Hibino, M. Miyayania, T. Kudo, *Solid State Ionics*, 2000, **134**, 271.
- M. R. Waller, T. K. Townsend, J. Zhao, E. M. Sabio, R. L. Chamousis, N. D. Browning and F. E. Osterloh, *Chem. Mater.*, 2012, **24**, 698.
- Martin Feneberg *et al.*, *Phys. Rev. B*, 2014, **90**, 075203.
- S. Ghosh, M. Saha and S. K. De, *Nanoscale*, 2014, **6**, 7039.
- L. Brus, *J. Phys. Chem.*, 1986, **90**, 2555.
- V. B. Kumar and D. Mohanta, *Bull. Mater. Sci.*, 2011, **34**, 435.
- S. Ghosh, M. Saha, V. D. Ashok, B. Dalal and S. K. De, *J. Phys. Chem. C*, 2015, **119**, 1180.
- A. M. Schimpf, N. Thakkar, C. E. Gunthardt, D. J. Masiello and D. R. Gamelin, *ACS Nano*, 2014, **8**, 1065.
- A. M. Funston, C. Novo, T. J. Davis and P. Mulvaney, *Nano Lett.*, 2009, **9**, 1651.
- H. Chen, L. Shao, Q. Li and J. Wang, *Chem. Soc. Rev.*, 2013, **42**, 2679.
- M. D. Malinsky, K. L. Kelly, G. C. Schatz and R. P. Van Duyne, *J. Am. Chem. Soc.*, 2001, **123**, 1471.
- P. K. Jain and M. A. El-Sayed, *J. Phys. Chem. C*, 2007, **111**, 17451.
- I. Kriegl, C. Jiang, J. Rodríguez-Fernández, R. D. Schaller, D. V. Talapin, E. da Como and J. Feldmann, *J. Am. Chem. Soc.*, 2012, **134**, 1583.
- A. Llordés, G. Garcia, J. Gazquez and D. J. Milliron, *Nature*, 2013, **500**, 323.
- J. Yin, C. Yue, Y. Zang, C-H. Chiu, J. Li, H-C. Kuo, Z. Wu, J. Li, Y. Fanga and C. Chena, *Nanoscale*, 2013, **5**, 4436.
- J-H. Lee, M-H. You, G-H. Kim and J-M Nam, *Nano Lett.*, 2014, **14**, 6217.
- S. Ghosh, K. Das, K. Chakrabarti and S. K. De, *CrystEngComm*, 2012, **14**, 929.
- A. Figuerola, M. v. Huis, M. Zanella, A. Genovese, S. Marras, A. Falqui, H. W. Zandbergen, R. Cingolani and L. Manna, *Nano Lett.*, 2010, **10**, 3028.
- R. Bose, A. H. M. Abdul Wasey, G P. Das and N. Pradhan, *J. Phys. Chem. Lett.*, 2014, **5**, 1892.
- B. K. Patra, A. Shit, A. K. Guria, S. Sarkar, G. Prusty and N. Pradhan, *Chem. Mater.*, 2015, **27**, 650.
- X. Chen, H-Y. Zhu, J-C. Zhao, Z-F. Zheng and X-P. Gao, *Angew. Chem. Int. Ed.*, 2008, **47**, 5353.
- S. Ghosh, S. Khamarui, M. Saha and S. K. De, *Rsc Adv.*, 2015, **5**, 38971.
- P. Christopher, H. Xin and S. Linic, *Nat Chem.*, 2011, **3**, 467.
- P. Christopher, H. Xin, A. Marimuthu and S. Linic, *Nat Mater.*, 2012, **11**, 1044.
- M. F. Saenger, T. Höing, B. W. Robertson, R. B. Billa, T. Hofmann, E. Schubert and M. Schubert, *Phys. Rev. B*, 2008, **78**, 245205.
- T. M. Mattox, A. Bergerud, A. Agrawal and D. J. Milliron, *Chem. Mater.*, 2014, **26**, 1779.
- C. G. Granqvist, *Solid State Ionics*, 1994, **70-71**, 678.
- L. Bartha, A. B. Kiss and T. Szalay, *Int. J. of Refractory Metals & Hard Materials*, 1995, **13**, 77.
- J-D. Guo, K. P. Reis and M. S. Whittingham, *Solid State Ionics*, 1992, **53-56**, 305.
- C. Yang, Q. Zhu, T. Lei, H. Li and C. Xie, *J. Mater. Chem. C*, 2014, **2**, 9467.
- X. Zhang, Y. L. Chen, R-S. Liu and D. P. Tsai, *Rep. Prog. Phys.*, 2013, **76**, 046401.
- Yan, S. C.; Li, Z. S.; Zou, Z. G. *Langmuir* 2010, **26**, 3894-3901.
- W. Sun, M. T. Yeung, A. T. Lech, C-W. Lin, C. Lee, T. Li, X. Duan, J. Zhou and R. B. Kaner, *Nano Lett.*, 2015, **15**, 4834-4838.
- G. Xi, J. Ye, Q. Ma, N. Su, H. Bai and C. Wang, *J. Am. Chem. Soc.*, 2012, **134**, 6508.

light irradiance in presence of Ag(5nm)/WO_{3-x} NHS catalyst is in the ESI, Fig. S15.

Figure Caption:

Fig. 1 (A) Large area TEM image of nearly monodispersed WO_{3-x} nanorods with length 85±10 nm and width 5.5±1.5 nm. (B) STEM-Dark field image shows the well dispersed nature of nanorods. (C) HRTEM image of three parallel aligned nanorods along the [200] zone axis. (D) SAED pattern of the nanorods. (E) Absorbance spectra of nanorods in 300 nm - 9000 nm region. Inset shows the Tauc plot ((αhν)² vs photon energy) in the UV-VIS region. (F) Tunability of the plasmonic absorption through variation of the refractive index (RI) of the solvent. The inset shows the LSPR λ_{max} as a function of refractive index. RI for CHCl₃, TCE, *o*-DCB, and CS₂ are 1.44, 1.51, 1.55, and 1.63, respectively.

Scheme 1: Schematic illustration of growth mechanism of WO_{3-x} nanorods.

Fig. 2 (A) XRD pattern of WO_{3-x} nanorods and different Ag/WO_{3-x} heterostructures. (B) Absorption spectra of as-synthesized WO_{3-x} nanorods and different Ag/WO_{3-x} heterostructures. Different color shaded area depicts the excitonic absorbance of WO_{3-x} (light cyan), metal plasmon absorbance (sandy brown), WO_{3-x} plasmon absorbance/ plasmon-plasmon coupling area (light green).

Fig. 3 (A) Large area TEM image of Ag(2nm)/WO_{3-x} nanoheterostructures shows each nanorod decorated with small sized (~ 2.5 nm) Ag nanocrystals. (B) A closer view of few Ag decorated WO_{3-x} nanorods. (C) TEM image of Ag(5nm)/WO_{3-x} heterostructures where each of nanorods decorated with 4-5 number of ~5 nm sized Ag nanocrystals. (D) A closer view of heterostructure, (E) STEM-DF image of the same. (F) A typical reconstructed HRTEM image at the site of interest. (G) masked FFT pattern of image (F) shows the presence of (020) plane of WO_{3-x} and (111) plane of Ag. (H) Simulated HRTEM shows the epitaxy between (111)_{Ag} and (020)_{WO_{3-x}} planes.

Fig. 4 (A) Large area TEM image of high quality Ag(10nm)/WO_{3-x} nanoheterostructure which shows each nanorods is attached with a single Ag nanocrystal. (B) HRTEM image of at WO_{3-x} and Ag connecting area. (C) FFT pattern obtained from green squared area in Fig (B) shows the pure WO_{3-x} phase. (D) Atomic model of WO_{3-x} along the [200] zone axis showing the planes obtained from FFT in Fig. (C). (E) FFT pattern obtained from blue squared area in Fig. (B) showing the presence of planes both from Ag and WO_{3-x}. Highlighted spots show the presence of (111) plane of Ag and (020) plane of WO_{3-x} along same direction. (F) Simulated HRTEM image by masking the highlighted spots of Fig. (E). (G) and (H) shows the atomic model of the matching of 2 d(020) of WO_{3-x} with 3 d(111) of Ag plane.

Fig. 5 Change of plasmon intensity of Ag nanocrystals during plasmonic photocatalysis process.

Fig. 6 Crystal structure of WO₃ along b-axis showing the intercalation of Ag(+1) ion in pseudo A-site of perovskite like structure.

Fig. 7 Left panel shows current-voltage plot of pure WO_{3-x} nanorods and different Ag/WO_{3-x} heterostructures. Right panel shows the temporal photo response of same at bias voltage 5V. Maximum photocurrent gain was obtained for Ag(10nm)/WO_{3-x} NHS.

Fig. 8 Relative band alignment of tungsten oxide and Ag.

Fig. 9 Light driven photodegradation of RhB and MB dye in presence of pure WO_{3-x} and different Ag/WO_{3-x} heterostructures. The change of absorbance of dyes during

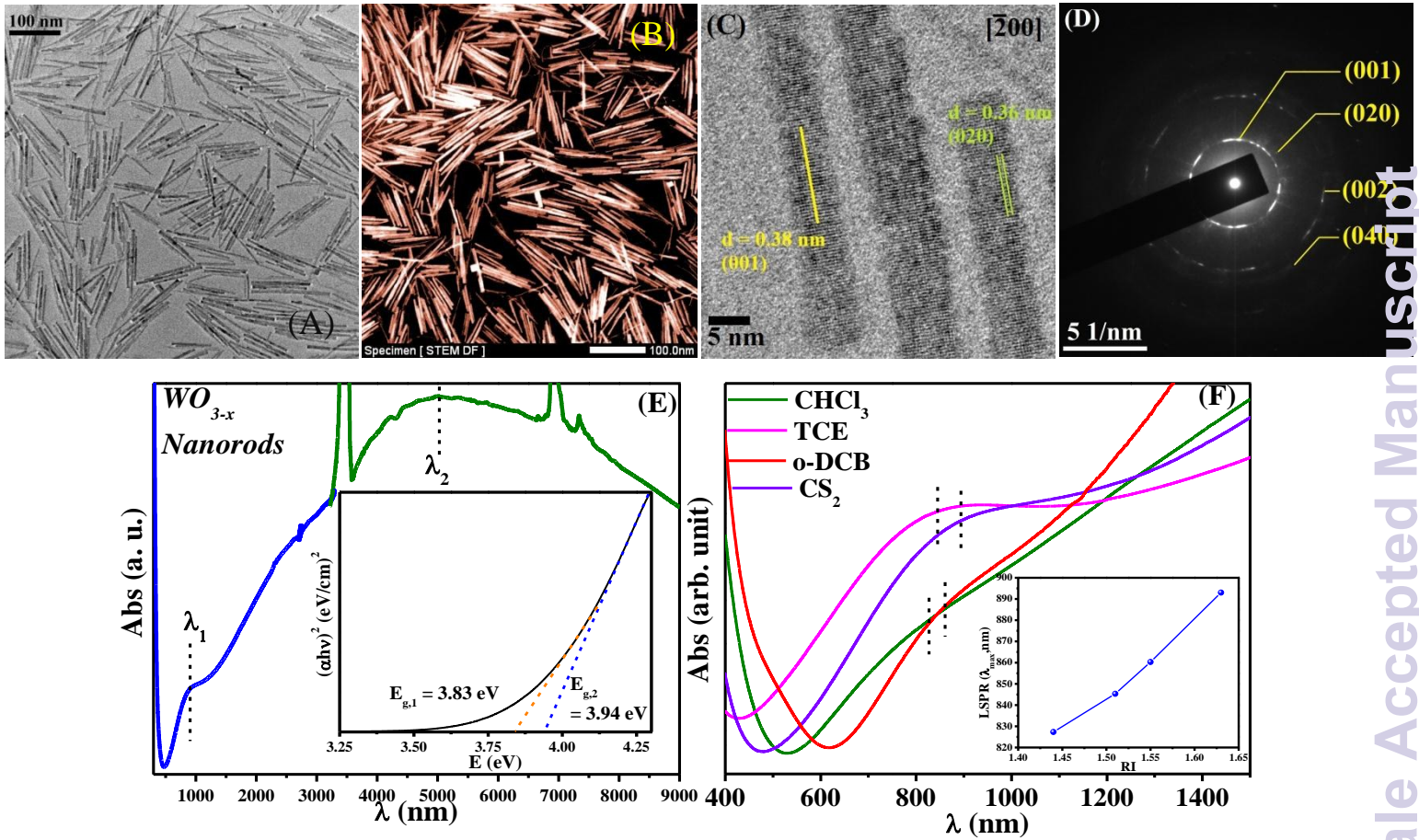


Fig. 1

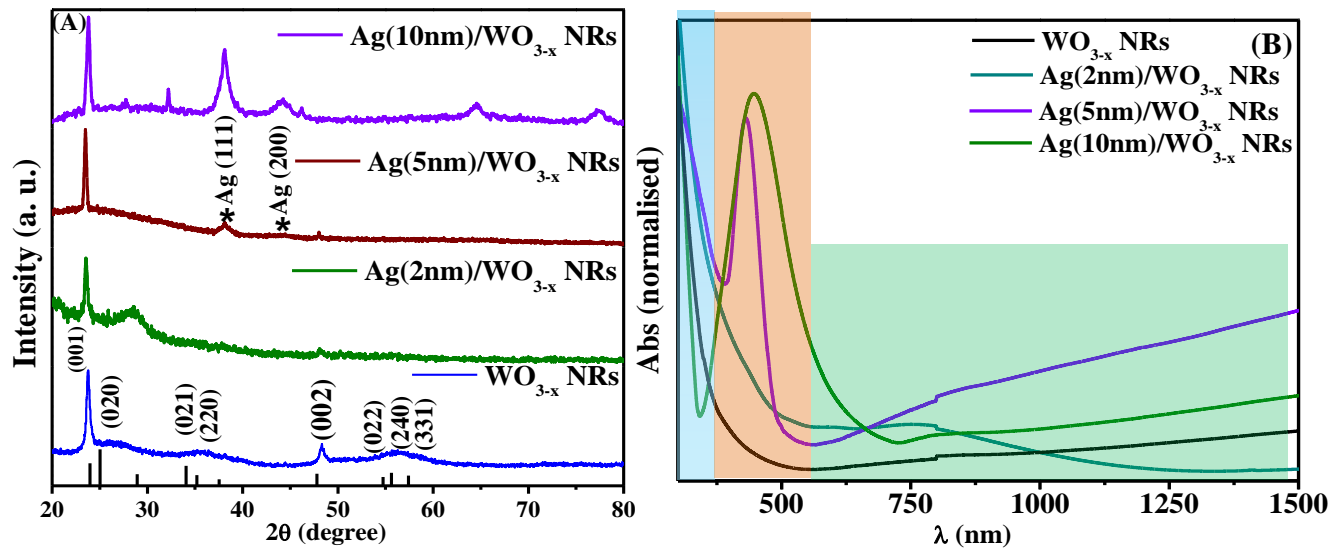


Fig. 2

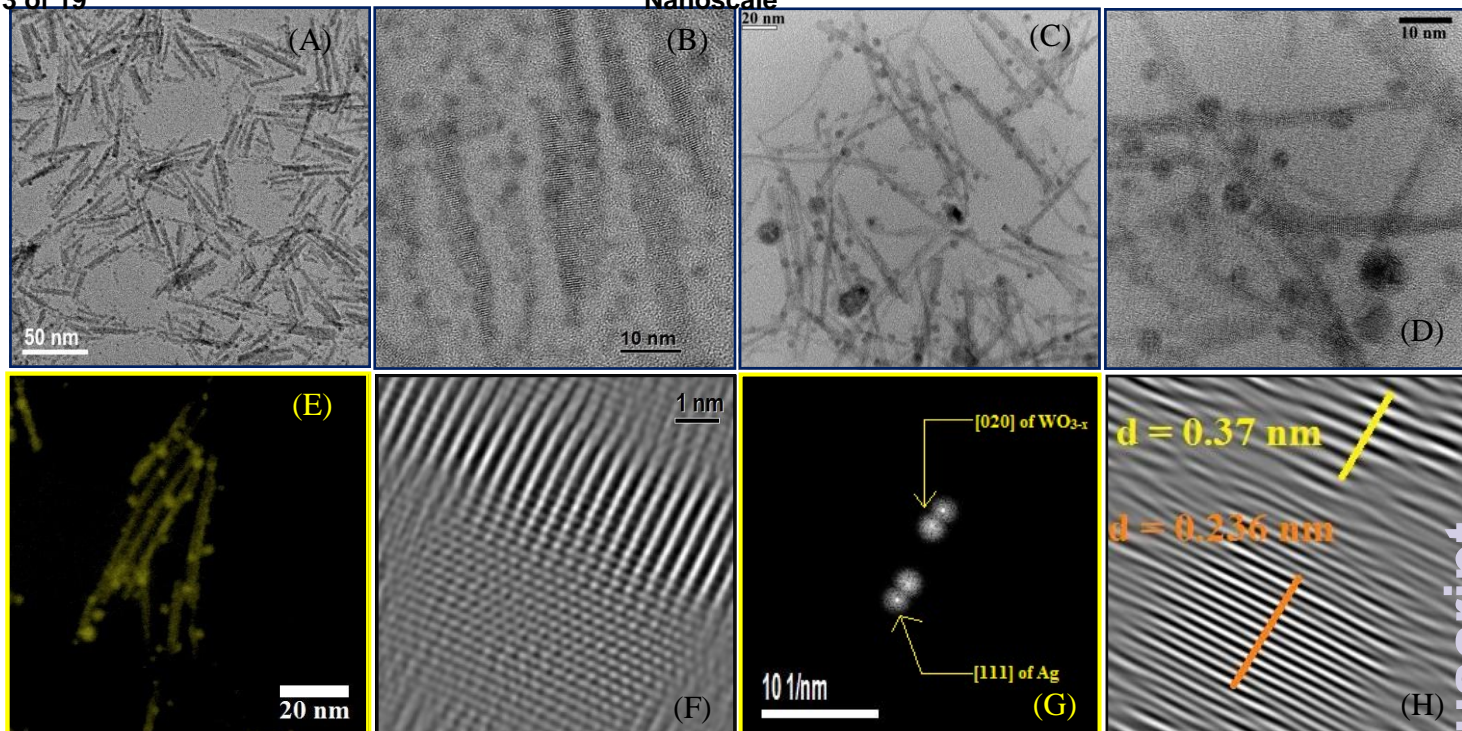


Fig. 3

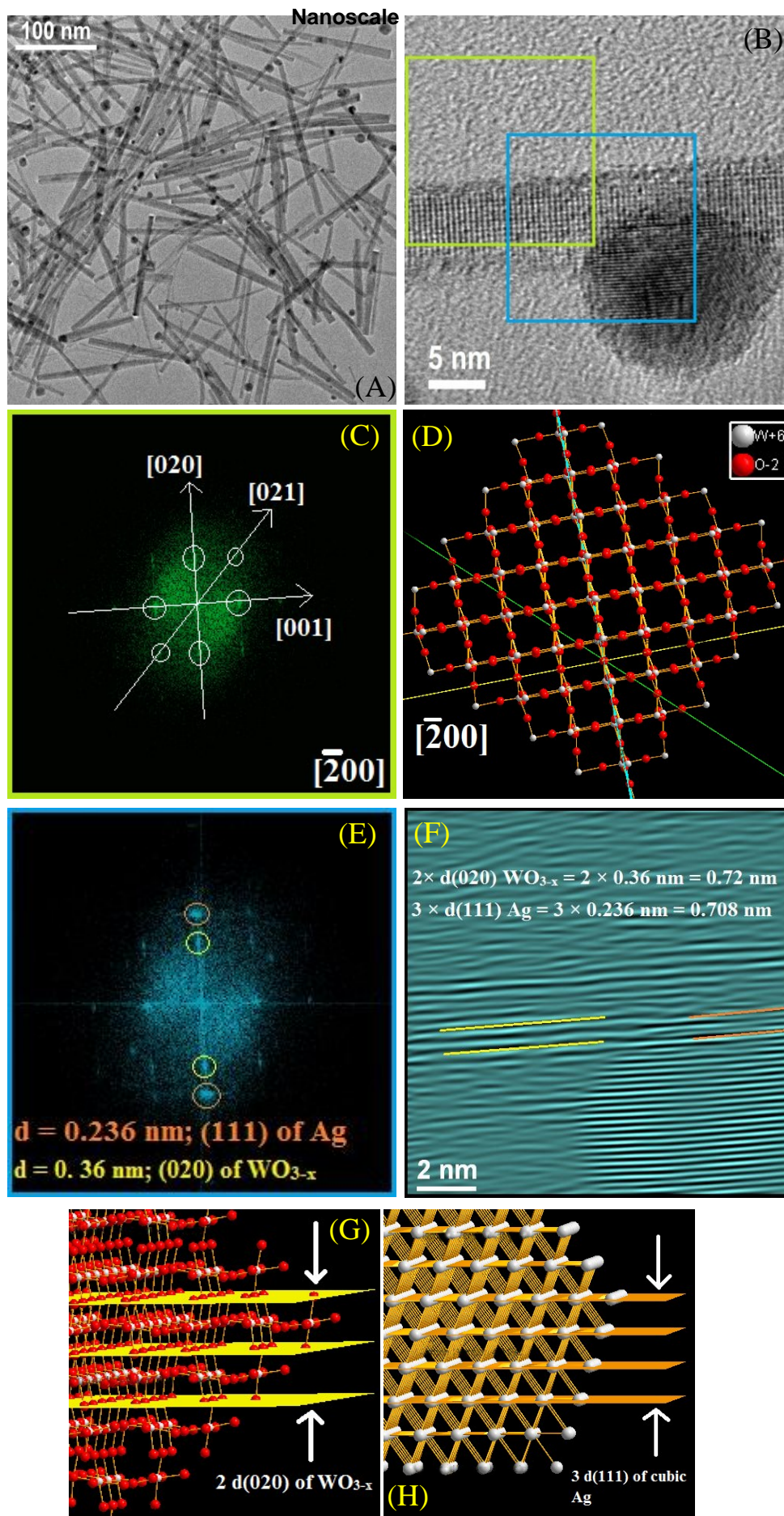


Fig. 4

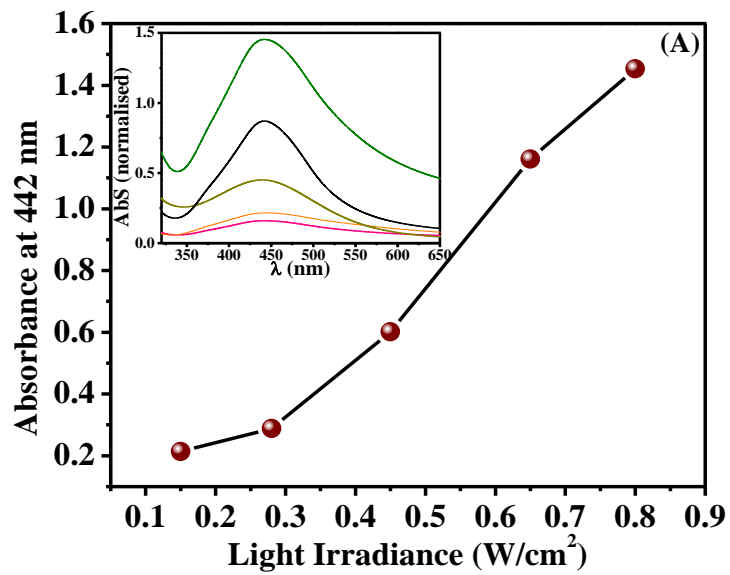


Fig. 5

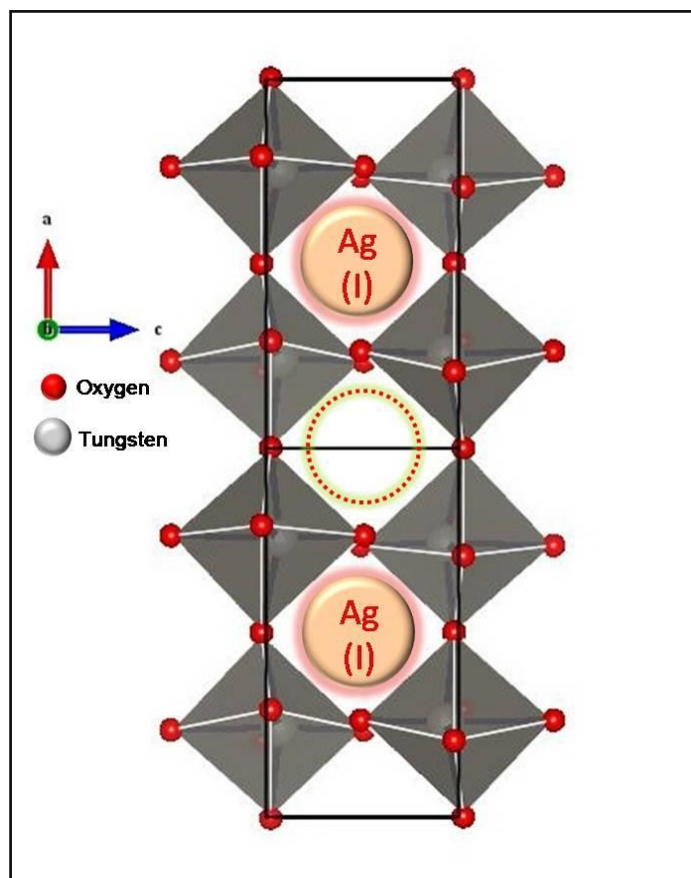
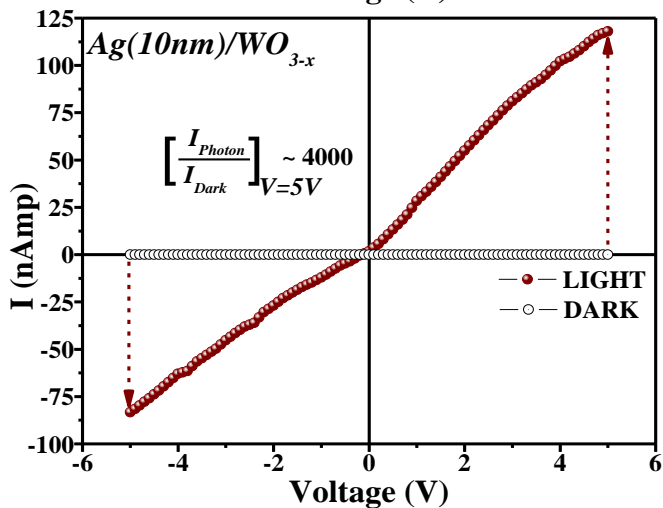
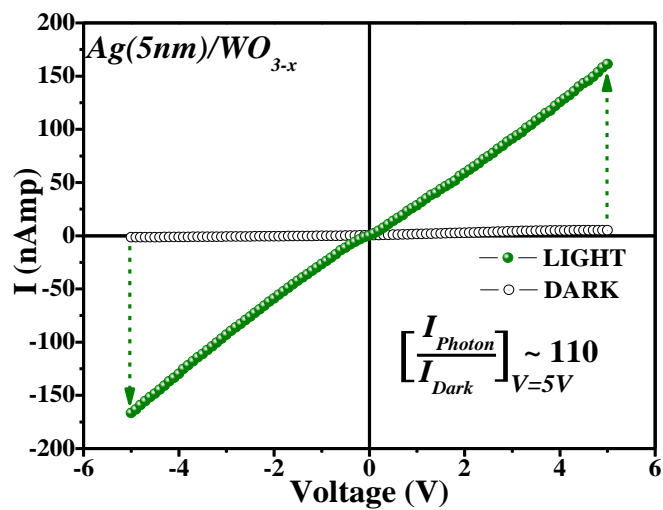
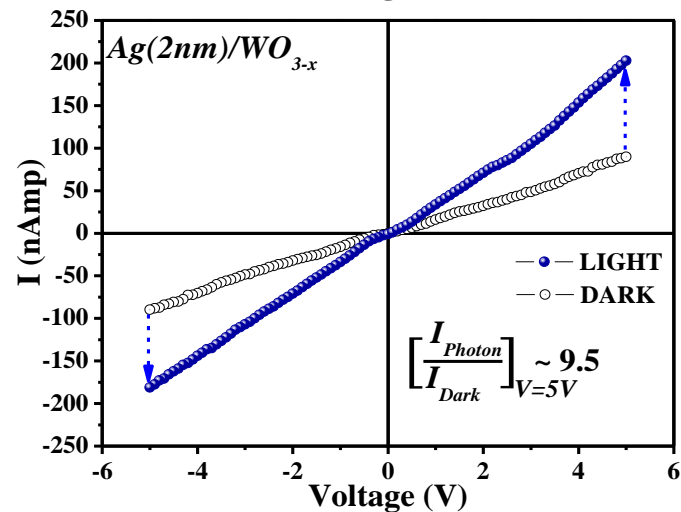
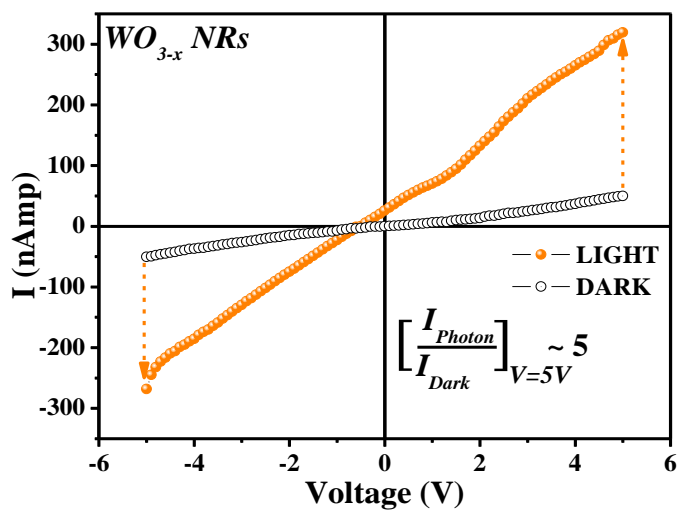
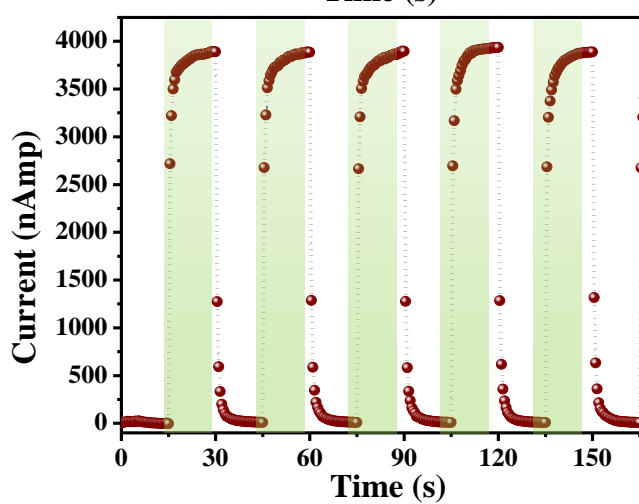
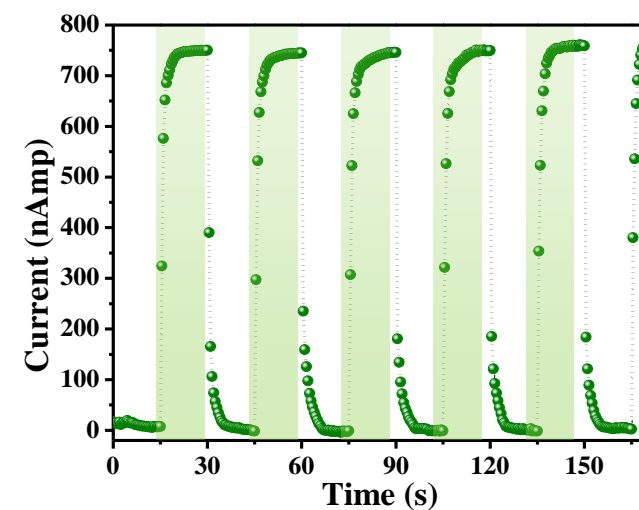
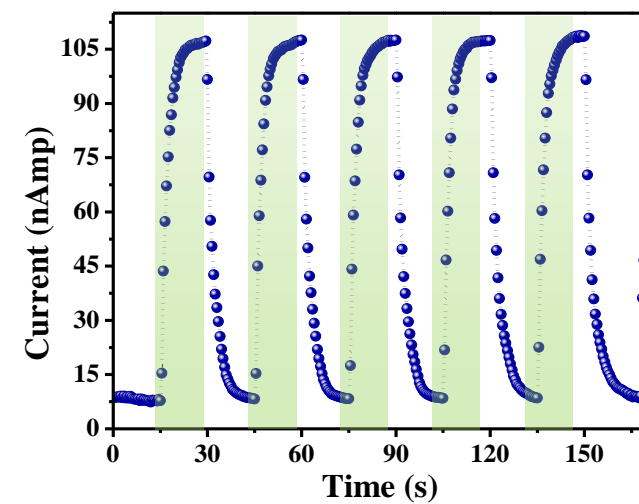
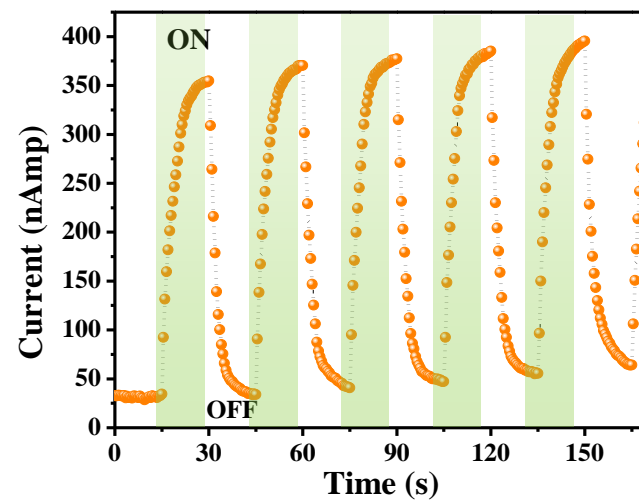


Fig. 6



Nanoscale



Nanoscale Accepted Manuscript

Fig. 7

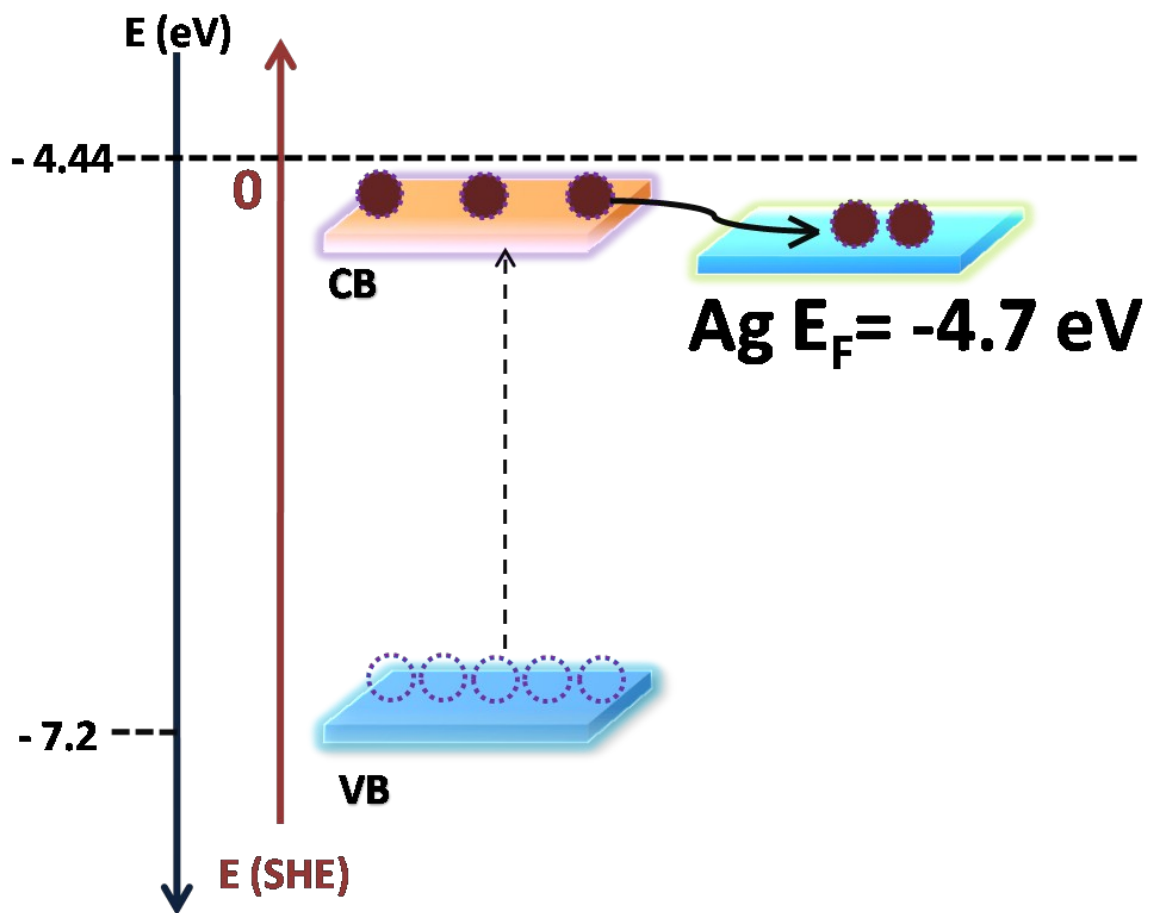


Fig. 8

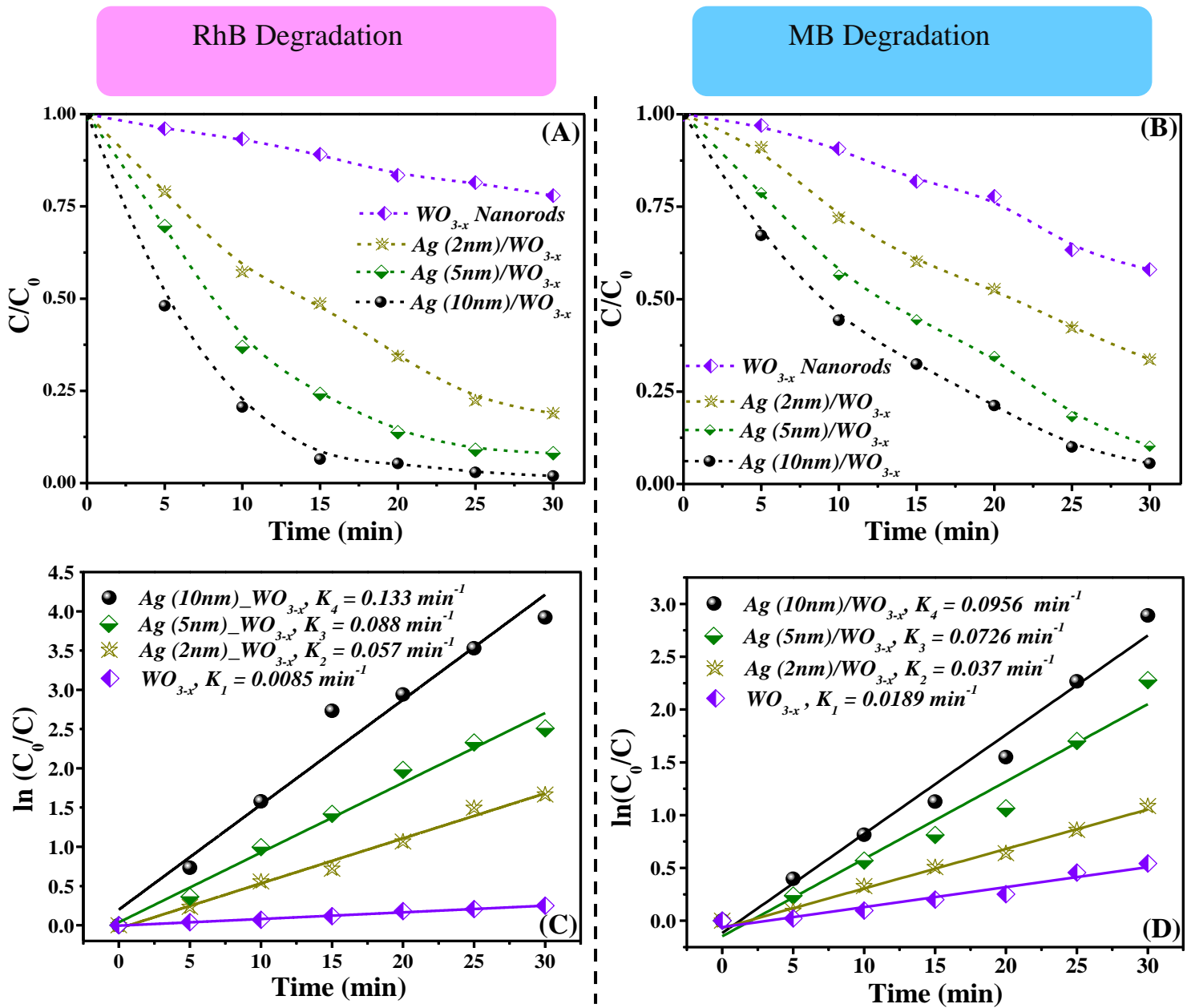
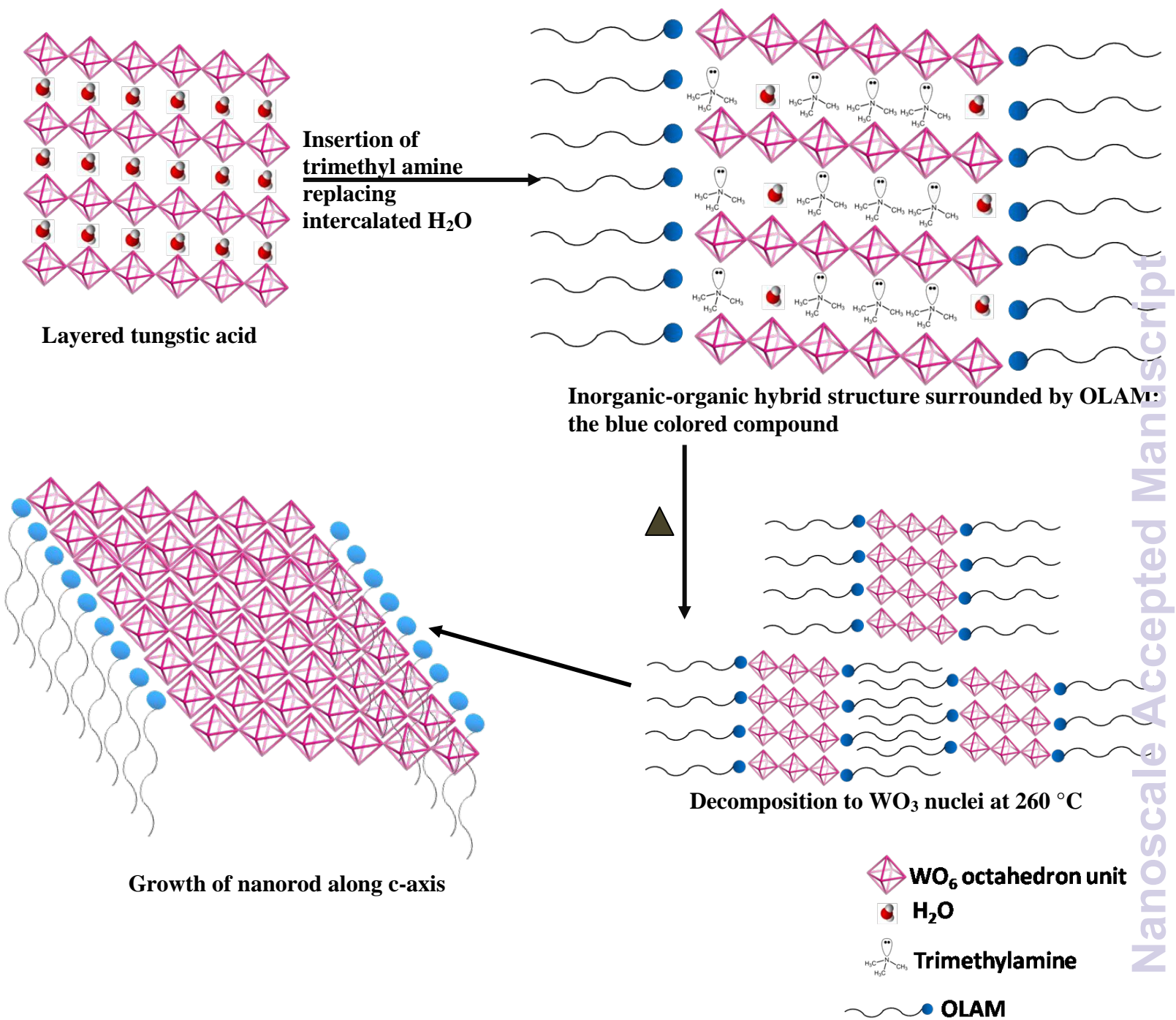


Fig. 9



Scheme -I